University of Bristol - Explore Bristol Research
General rights

In-situ X-ray Computed Tomography Characterisation of 3D Fracture Evolution and Image-Based Numerical Homogenisation of Concrete[1]

Z. Yang[1]*, W. Ren[2], R. Sharma[3], S. Mcdonald[4], M. Mostafavi[5], Y. Vertyagina[6] and T.J. Marrow[6]

[1]Centre for Low Impact Buildings, Faculty of Engineering & Computing, Coventry University, UK

[2]College of Water Resources and Architectural Engineering, Northwest A&F University, China

[3]School of Engineering, Indian Institute of Technology Mandi, India

[4]Manchester X-ray Imaging Facility, School of Materials, the University of Manchester, UK

[5]Department of Mechanical Engineering, University of Bristol, Bristol, UK

[6]Department of Materials, University of Oxford, UK

Abstract: In-situ micro X-ray Computed Tomography (XCT) tests of concrete cubes under progressive compressive loading were carried out to study 3D fracture evolution. Both direct segmentation of the tomography and digital volume correlation (DVC) mapping of the displacement field were used to characterise the fracture evolution. Realistic XCT-image based finite element (FE) models under periodic boundaries were built for asymptotic homogenisation of elastic properties of the concrete cube with Young's moduli of cement and aggregates measured by micro-indentation tests. It is found that the elastic moduli obtained from the DVC analysis and the FE homogenisation are comparable and both within the Reuss-Voigt theoretical bounds, and these advanced techniques (in-situ XCT, DVC, micro-indentation and image-based simulations) offer highly-accurate, complementary functionalities for both qualitative understanding of complex 3D damage and fracture evolution and quantitative evaluation of key material properties of concrete.

Key words: X-ray computed tomography, Fracture, Segmentation, Digital volume correlation, Homogenisation, Concrete

---

*Corresponding author: Prof. Z Yang, Email: ac1098@coventry.ac.uk

1 INTRODUCTION

Quasi-brittle multiphase composite materials, such as concrete, bones, fibre-reinforced plastics (FRP) and ceramic/metal matrix composites are widely used in engineering structures of many industries. A better understanding of their mechanical behaviour can lead to development of materials with higher load resistance, cost-effective manufacturing processes and optimal structural designs. Due to the random distribution of multiple phases from the nano-, micro-, meso- to macro-scales, multiphase composite materials have intrinsically heterogeneous and nonlinear mechanical properties, which in turn directly determine the performance and reliability of structures and systems. Therefore, understanding their mechanical properties including damage and fracture at different scales, through both experimental studies and computational modelling, becomes one of the most critical and challenging engineering and scientific problems (Oden et al., 2003; Kassner et al., 2005).

The X-ray computed tomography (XCT) technique, a 3D imaging technique originally used in medicine, is now widely used to characterise the internal nano/micro/meso-scale structures of many materials, because of its high resolution, non-destructive nature, and ability to clearly visualise details including different phases, interfaces, pores and cracks. For instance, in the last decade XCT has been applied to characterise microstructures and properties of wide range of materials, such as geological materials (rock, soil and fossils) (Carlson, 2006), metals and alloys (Babout et al., 2006; Marrow et al., 2006; Qian et al., 2008), porous materials (Kerckhofs et al., 2008), composites (Drummond et al., 2005; Sharma 2013), asphalt mixtures (Song et al., 2006), cement (Meyer et al., 2009) and concrete (Garboczi, 2002; Wang et al., 2003; Man and van Mier, 2008; Landis and Bolander, 2009). Many XCT studies acquire the internal structures of intact materials without external loading, or study damaged materials after loading (i.e. post-mortem analyses). However, in-situ XCT studies, which scan the internal structures of materials under progressive loadings so that the structural damage and fracture evolution can be examined and related to the loading process are now feasible. For example, De Kock et al (2015) have observed the fracture process in rocks under ambient freeze−thaw cycling and Nagira et al (2011) studied semi-solid carbon steels., whilst in recent years some of the authors of this paper have conducted in-situ XCT experiments to examine deformation in metal-metal composites (Baimpas et al., 2014), fatigue cracking in magnesium alloy (Marrow et al., 2014), indentation cracking in alumina (Vertyagina et al., 2014) and ceramic composites (Saucedo-Mora et al (2016)), tensile deformation in nuclear graphite (Marrow et al., 2016), and polymeric foams (McDonald et al. 2011), liquid flow and deformation in semi-solid aluminium alloys (Cai et al, 2016), indentation deformation in a metal-matrix composite

---

*Corresponding author: Prof. Z Yang, Email: ac1098@coventry.ac.uk

(Mostafavi et al, 2015), and fracture of propagation in nuclear graphite (Mostafavi et al, 2013). For such studies to be successful, it is important to consider the experimental constraints of increasing X-ray absorption with sample dimension and density, which limits the maximum dimensions and increases the time to record tomographs, and also for digital volume correlation analysis of deformation, it is necessary that the microstructure contains sufficient "speckle" contrast that can be discerned at the experiment's resolution (Bay et al, 1999).

One particularly attractive research direction is to build micro/meso-scale finite element (FE) models from the high-resolution XCT images. As these FE models describe the original heterogeneous micro-structures, including the shape, size and distribution of each phase, they can be more realistic and accurate than micro/meso-scale models with assumed structures. These XCT image-based FE models, after being fully validated against experiments, may be used to optimise the micro-structures of a material for user-specified properties without the need of complicated and costly experiments. However, 3D XCT images have only occasionally been used to build geometrically realistic FE models, for example, by Hollister and Kikuchi (1994) for trabecular bones, Terada et al. (1997) for metal matrix composites, McDonald et al. (2011) for foams, Sharma et al (2013) for carbon/carbon composites, Man and van Mier (2008) for concrete, and more recently Qsymah et at. (2015) for fibre reinforced concrete and Saucedo Mora et al. (2016) for a ceramic-matrix composite

In this study, both in-situ micro XCT tests of concrete cubes under progressive compressive loading and XCT-image based FE modelling are carried out, to gain a better understanding of the 3D fracture mechanisms and mechanical properties of concrete. Two methods are used to characterise the fracture evolution considering the unique multi-phasic internal structure of concrete. The first segments the attenuation contrast of XCT images (using AVIZO (2013) software) into different phases, namely, aggregates, cement, cracks and voids. The second uses the digital volume correlation (DVC) technique to map the relative deformations between consecutive XCT images with high precision; bulk mechanical properties are measured from the displacement field and cracks visualised via the apparent strain of their opening displacement. The 3D crack profiles obtained by these two methods are compared. The XCT-images are then transformed into 3D FE models to calculate the bulk material properties using the asymptotic homogenisation technique with periodic boundary conditions. The elastic moduli of aggregate and cement, required as inputs for the FE models, are obtained by micro-indentation experiments. The elastic moduli of the concrete cube, obtained from the in-situ test, the DVC study, the FE homogenisation and the theoretical bounds (Hill, 1952), are compared, in order to validate the FE modelling as well as to

clarify uncertainties in the recorded load-displacement curves by the in-situ loading rig.

2 EXPERIMENTAL STUDIES AND ANALYSES

2.1 In-situ XCT tests

The in-situ XCT tests were carried out at the Manchester X-ray Imaging Facility (MXIF), the University of Manchester, UK, using the 320 kV Nikon Metris custom bay, as shown in Fig. 1a. The loading rig, consisting of a Deben micro-test stage supporting a transparent cylinder, was mounted on the circular stage of the XCT machine. 40 mm concrete cubes were cast with a target cylinder compressive strength of 15 MPa and a mix ratio of 1.0 cement : 0.6 water : 4.0 aggregates in mass. The strength and the size of specimens were chosen so that the specimens could be loaded to failure by the loading rig, which had a loading capacity of 25 kN, and also to ensure sufficient X-ray transmission to obtain high resolution tomographs. The cement was ordinary Portland cement. The aggregates were gravels with an average size 5 mm. No fine aggregates (i.e. sand) were used to ensure a relatively simple micro-structure.

Two steel pads, glued by double-side adhesive tapes to the centre of the top and bottom surfaces of the specimen, provide a loading area of 17.5 mm×17.5 mm (i.e. 19% of the sample cross-section area) to achieve a vertical splitting failure. They were centred inside the enclosing transparent cylinder for tests, as in Fig. 1b, where a failed concrete specimen is also shown.


(a): The in-situ XCT facility in MXIF   (b) A specimen after failure

Fig. 1 Setup of the in-situ XCT test

Fig. 2 illustrates the in-situ XCT test procedure. The 1st scan was conducted without loading. The load was then applied via compression at a displacement rate of 0.5 mm/min to 2.5 kN, at which point the 2nd scan was carried out. The specimen was then reloaded to 6 kN at the same rate and the 3rd scan was done. The 4th scan was conducted similarly at 10 kN and the 5th at 16.5 kN, after which

a wide crack was noticeable. The unloading data could not be recorded reliably.

Following some optimisation of the parameters, each X-ray scan was conducted with 160 kV and 60 μA intensity. For each scan, the stage was rotated by 360°, resulting in 2000 2D radiographs with pixel resolution 37.2 μm; it took about 2 hours for each scan to complete. The 2D radiographs were reconstructed into 3D absorption contrast images using the CT Pro and VG Studio software. Image defects such as beam hardening and ring artefacts were removed by post-processing with standard methods in the CT Pro software. Each 3D data set was initially about 15 Gb in size. To reduce the data processing time, the 3D data volumes were cropped to cubes of side 37.2 mm (i.e. 1000 pixels in each dimension). This reduced the data size to 2 Gb for each scan, with the bit depth also reduced from 32 bit float to 16.
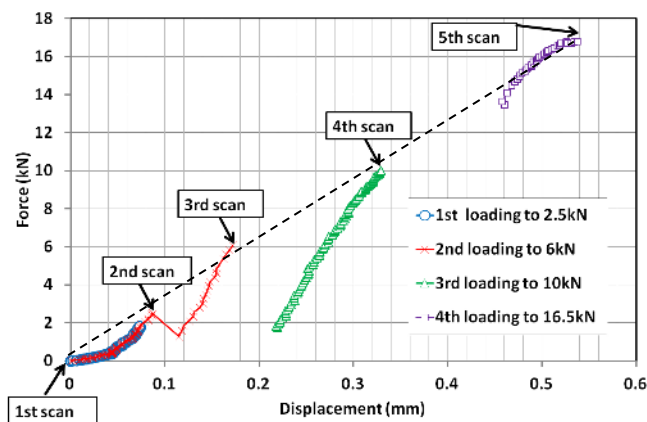
Fig. 2: The in-situ XCT test procedure with load – displacement shown

2.2 Visualisation and segmentation

A 2D section of the XCT data is shown in Fig 3. The aggregate, large pores and cement are readily observed, and the crack is also discernable. The software AVIZO (2013) was used to visualise the 3D crack evolution during loading, and segment the XCT images into different phases for qualitative and quantitative analyses, and image-based numerical modelling. A segmentation procedure was developed and outlined below using the images at 16.5 kN as an example.
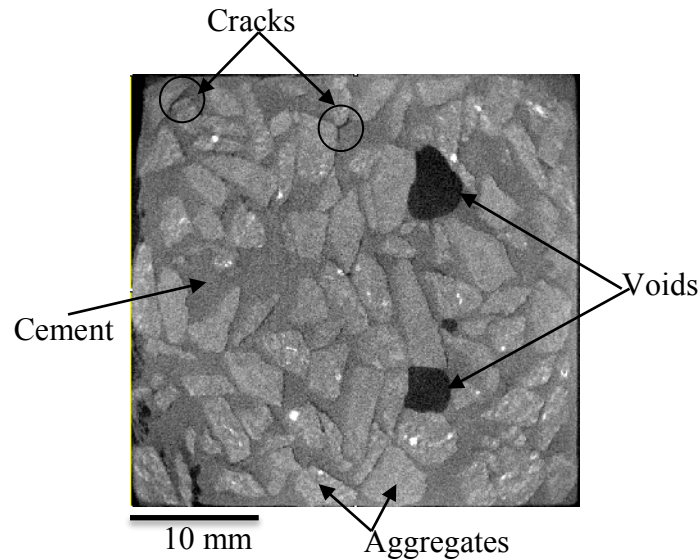
Fig. 3 A 2D grey scale section of an XCT image (before loading)

2.2.1 Determination of thresholds for phases

The Line-Probe command was used to determine a proper threshold of grey value (i.e. absorption contrast) to segment each phase in the XCT attenuation image; Fig. 4 shows an example. The sensitivity to location was examined to verify that the threshold values reliably segmented each phase. The full grey scale is 0~65535 (16 bit image), and the chosen threshold was >33000 for aggregates, <19000 for voids and cracks; values between them were identified as cement.

2.2.2 Segmentation

The thresholds are then used in AVIZO to segment the XCT images into three phases (cement, aggregate, voids and cracks) under different loadings. However, using thresholds alone to segment microstructures is unreliable, due to issues from connected aggregates and missed areas ("islands"). As the objective was to extract an image-based 3D model of the microstructure, a series of manual operations on the 2D slices were carried out to supplement the initial assignment of microstructures by thresholding. This included separation of connected aggregates and addition of missed areas. Fig. 5a and Fig. 5b show the segmented aggregates, voids and cracks on a typical slice, respectively. The segmented cement is shown in Fig. 5c, obtained by an image operation that subtracts aggregates, cracks and voids from the original image. A full description of the segmentation procedure can be found in (Li, 2012).
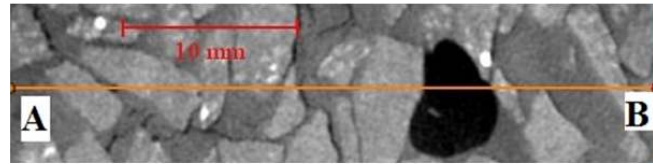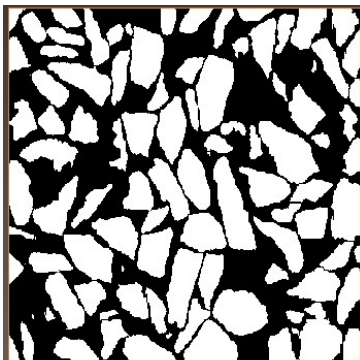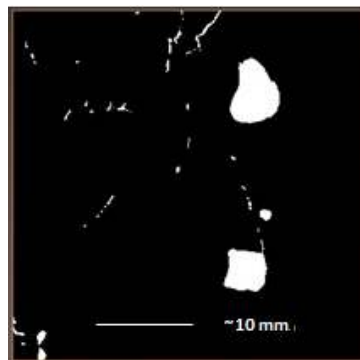
a) Line-probe path AB
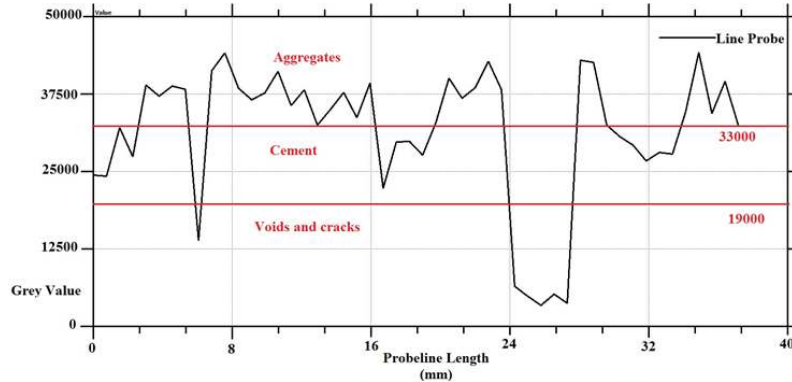
b) Variation of grey values along AB

Fig. 4: Determination of thresholds for different phases

a) aggregates in white   **b)** voids and cracks in white   **c)** cement in grey
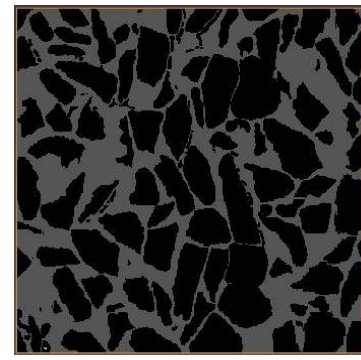
Fig. 5: Segmented phases from XCT image

2.2.3 Visualisation of three phases and fracture evolution

From the set of segmented 2D image slices, the 3D shape and distribution of aggregates, cement, voids and cracks can be visualised, as shown in Figs 6a-c. The combined concrete structure of the specimen without load is shown in Fig. 6d. The segmented cracks and voids, the combined concrete and the failed specimen at the peak load 16.5 kN are shown in Fig. 7a, 7b and 7c respectively. The segmentation of cracks is based on the threshold of grey values (19000 in Fig. 4) and is thus not entirely objective, and there also exist initial cracks in the unloaded specimen as shown in Fig. 6c. The major cracks on the specimen surface in Fig. 7b are aligned approximately vertically, which is

7

typical of concrete specimens under splitting tests.

Comparison of Fig. 6c and Fig. 7a demonstrates that a large number of 3D cracks propagate, leading to a very complicated crack pattern during loading. Although the specimen geometry, loading and boundary conditions are all symmetric, the crack pattern is not symmetric. This reflects the effects of the random distribution of aggregates and thus the heterogeneous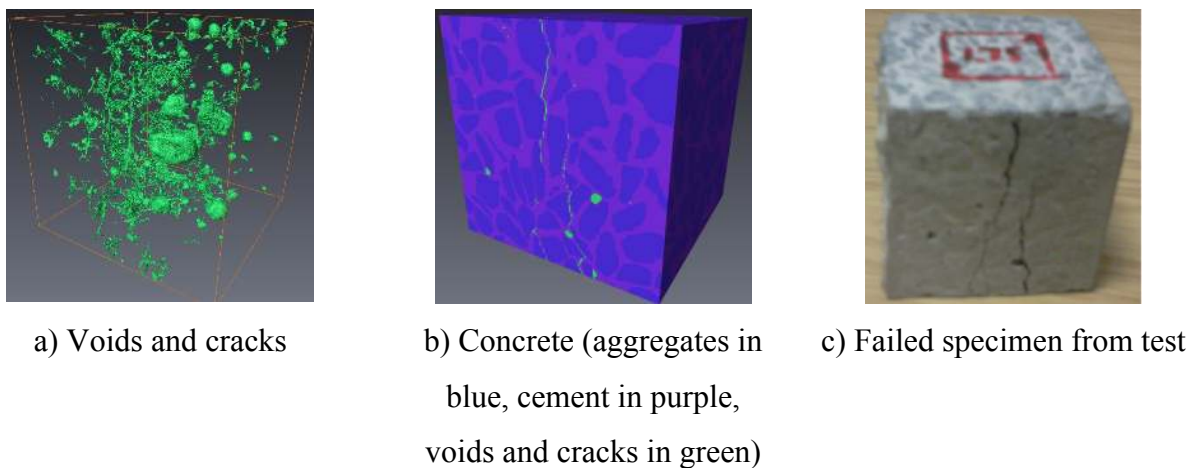 nature of mechanical properties of concrete. More detailed examination of 2D slices reveal that the cracks first propagate along aggregate-cement interfaces, which are then bridged by cracks in the cement to form the macro-cracks.

Statistical analyses based on the segmented cube were carried out. The volume fraction of aggregates, cement, and voids/initial cracks observed in the sample without load is 49.6%, 49.3%, and 1.1%, respectively. The mean value of volume, length, width and equivalent diameter of all aggregates is 39.1 mm^3, 7.4 mm, 2.7 mm and 3.9 mm, respectively, indicating the complicated random geometry of aggregates.

a) Aggregates   b) Cement   c) Voids and cracks   d) Concrete (aggregate in green, cement in blue and voids in purple)
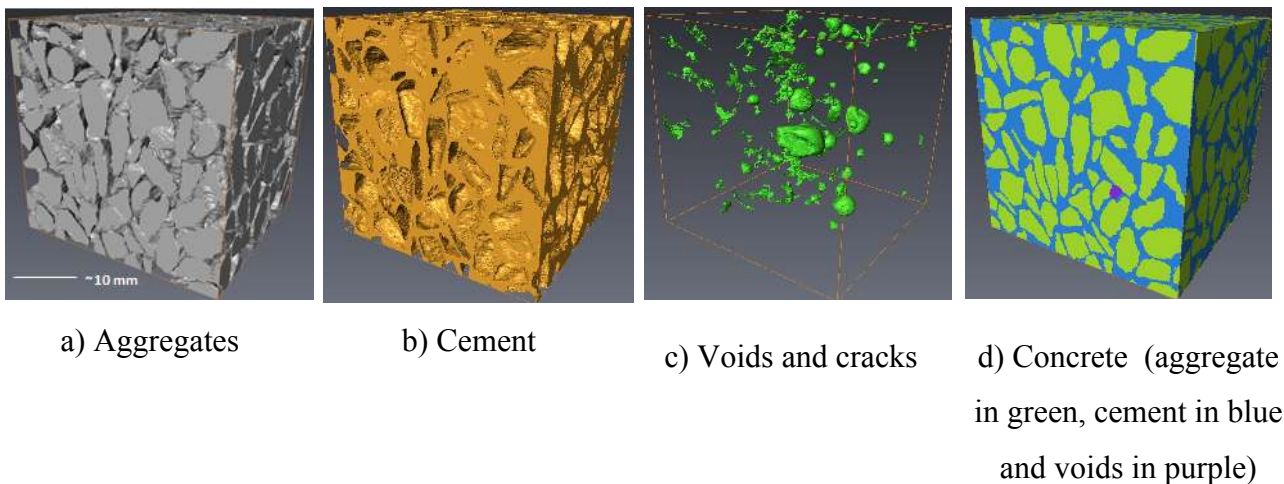
Fig. 6: 3D Segmented phases without load.

a) Voids and cracks   b) Concrete (aggregates in blue, cement in purple, voids and cracks in green)   c) Failed specimen from test

Fig. 7: 3D segmented voids and cracks, combined concrete and failed specimen at peak load

The calculated volumes of the voids and cracks under different loads are shown in Fig. 8. The volume decreases as the load increased to 10 kN, which is attributed to compaction of the concrete under compression. As the load increases to 16.5 kN, a higher volume of cracks and voids is observed, which is due to initial cracks gradually propagating and new cracks forming. Shortly above this peak load, major vertical cracks propagate rapidly, leading to significant dilation in the specimen.
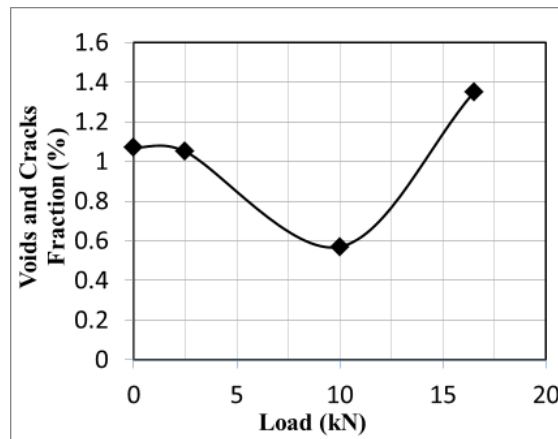
**Fig. 8:** Evolution of cracks and voids

2.3　Digital volume correlation

Measurement of the elastic modulus of the cube from the load and machine displacement is not possible due to the loading rig's compliance; it was not possible to introduce an extensometer or strain gauge due to the setup for XCT. The measured vertical stiffness of the cube, using the slope of the dashed line in Fig. 2 up to 10.5 kN, gives a modulus of 0.85 GPa which is far lower than the expected elastic modulus of 20-30 GPa of normal-strength concrete; this is largely due to the compliance of the loading rig. The 3D digital volume correlation (DVC) technique (Bay et al., 1999; Mostafavi et al., 2013a; Mostafavi et al., 2013b; Vertyagina et al., 2014) was therefore applied to measure the full 3D displacement field within the cube, from which the average strain and elastic properties in the loaded volume could then be obtained (Baimpas et al., 2014; Gonzalez et al., 2013; Marrow et al., 2016).　In addition, like 2D digital image correlation (DIC), crack opening displacements less than the voxel size can be detected and measured by DVC, and thus cracks that are too narrow to be detected by threshold-based segmentation of the XCT image can also be identified (Marrow et al., 2012; Vertyagina et al., 2014).

The DVC analyses were carried out using the LaVision Davis software (DaVis, 2012). In the 1st

analysis, a large interrogation window size (128×128×128 voxels with 2 passes and 50% overlap) was used to calculate the overall distribution of displacements. In a 2nd analysis a smaller interrogation window was selected (64×64×64 voxels). Reducing the interrogation window increases the spatial resolution of the displacement field, which is useful for visualisation of cracks, but it also increases random errors. A 3rd analysis using 32×32×32 voxel was also conducted to visualise the damage with higher resolution.

To improve measurement precision of bulk deformation, the displacements due to rigid body translation and rotation, which inevitably occur during mechanical loading, were decoupled from those resulted from deformation. This was done by identifying the Euler rotation angles and applying a reverse rotation to the DVC-measured displacement field at 128×128×128 voxels (i.e. the most precise dataset); the details of this method are described in (Mostafavi et al., 2015). The measured rotations of the sample in all loadings were found to be of the order of 0.5°. The vertical displacements over the area of the loading plates were averaged at the top and bottom of the tomographed region specimen (separated by a gauge distance of 38.92 mm); the difference between them is the vertical compressive displacement of the sample for each loading sequence, as shown in Fig. 9. The elastic modulus calculated from the dashed line in Fig. 9 for the first three loading sequences in which no extended cracks were observed, is 26.42±3.20 GPa. The increase in stiffness at higher load may be attributed to the complex behaviour of the specimen as cracking develops.
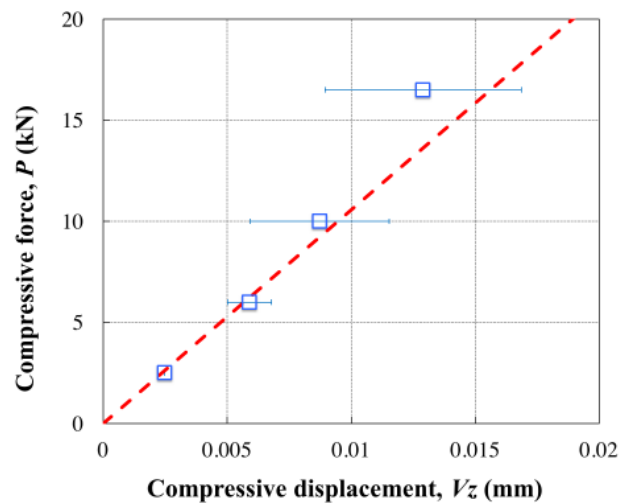
Fig. 9: Load-displacement curve from XCT and DVC.

Fig. 10 shows a comparison of a series of XCT and DVC data, in a vertical slice near the specimen centre, as the load is increased from 2.5 kN (left) to 16.5 kN (right). The DVC data show the nominal maximum principle or normal strain (these visualisations use the 32×32×32 subset data for higher resolution). The maximum normal strain is a measure of the crack opening displacement

10

magnitude, and reveals the complex pattern of cracking in a more sensitive manner than the segmentation of the XCT data. Some artefacts due to image correlation errors associated with the edges of large pores can be seen in the DVC data. The tomograph obtained at 2.5 kN is slightly blurred compared with the others; this may be due to sample movement during the scan, most likely from crack propagation. The blurring affects the DVC analysis, and the resulting errors affect the produced local uncertainties in the gradients of the displacement field. This appears in the DVC strain map at 2.5 kN as increased local strains, which are absent in the analysis of the better quality tomographs. The strain is a measure of the displacement change across the crack, and the strain dataset obtained by DVC can be segmented using a strain threshold, in a similar manner to the grey-scale segmentation of the attenuation XCT images.

An example of a semi-quantitative 3D visualisation of the crack, obtained by segmentation of the maximum principal strain field data at 16.5 kN is shown in Fig. 11; the hotter colours (red) represent higher crack opening displacements. The dataset is that obtained with the 64×64×64 voxel subsets, and the strain segmentation threshold is 0.25. The surface profile is not defined with very high resolution due to 32 voxel separation between the displacement vector data, but the crack path is continuous and more completely defined than that obtained by segmentation of the XCT data (Fig. 7). The DVC analysis also discriminates between the crack (which opens) and voids (which do not open), unlike segmentation of the XCT data alone.
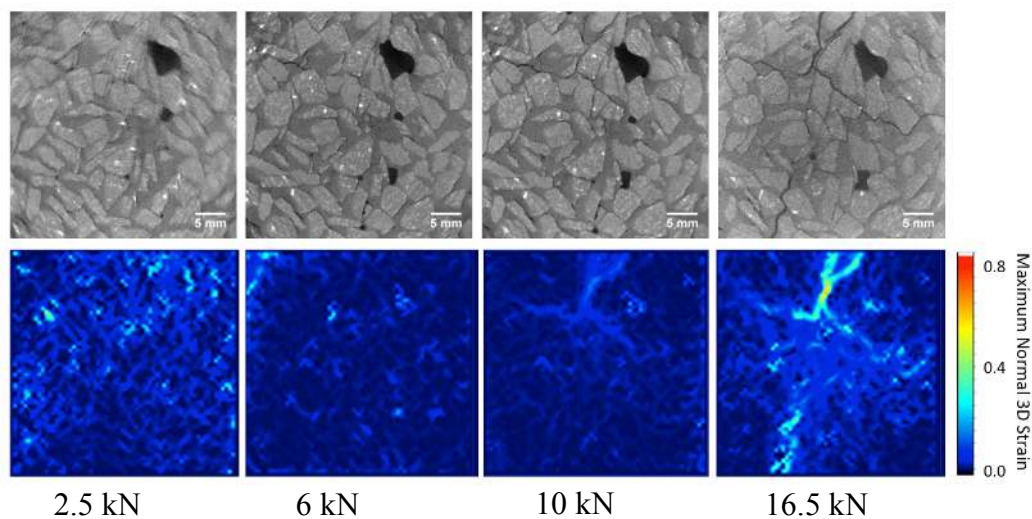
Fig. 10: Fracture evolution in a vertical slice; by XCT (top) and DVC (bottom), as the applied load increases from left to right
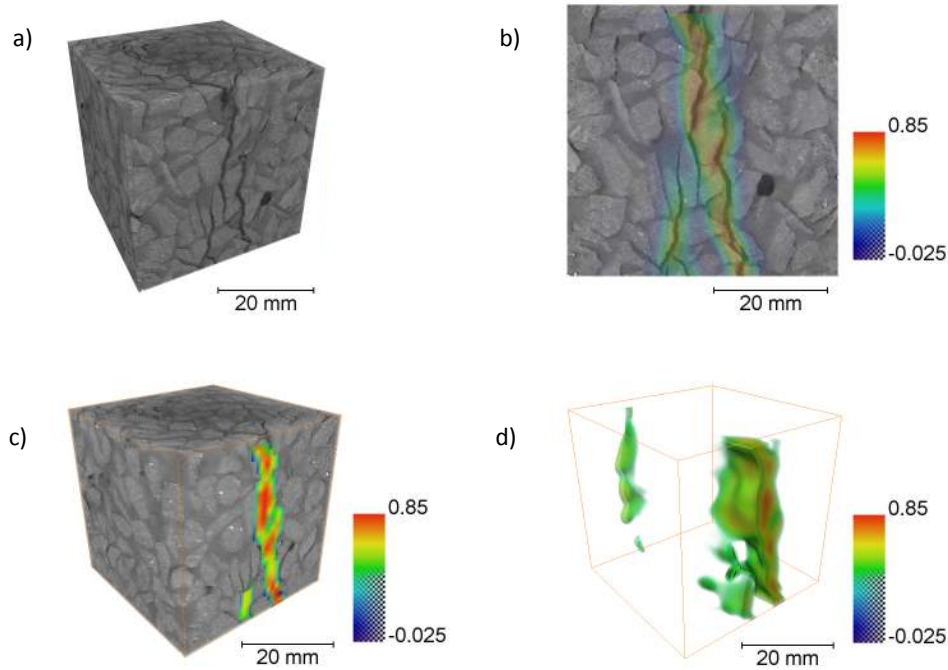
Fig. 11: Segmentation of 3D cracks at 16.5 kN, using DVC-measured nominal maximum principle strains: a) attenuation tomograph of damaged specimen; b) superposition of strain map on 2D slice of tomograph; c) superposition of 2D slice of strain map on 3D tomograph; d) 3D visualisation of 3D strain map.

2.4   MICRO-INDENTATION TESTS

Micro-indentation tests were carried out to measure the Young's moduli of aggregates and cement and hence estimate the global elastic modulus of the concrete cube. The measurements were done using a CSM micro-indentation tester with Vickers diamond indenters. Two concrete specimens of $20 \times 10 \times 10$ mm^3 and $20 \times 20 \times 10$ mm^3 were cut from the 40 mm concrete cube. They were then ground and polished using silicon carbide abrasive papers up to 6.5 μm and diamond particles of suspensions up to 1 μm to achieve highly flat surfaces. Finally, the specimens were cleaned by alcohol and distilled water to remove dust and diamond particles left in the voids and porous areas before the indention tests.

A constant linear loading rate was used until the applied force reached a specified value (0.1 N, 0.3 N, 0.5 N, 0.8 N and 1.0 N) for each tested point. The load was then held for 10 seconds before unloading at the same rate before next point was tested. The distance between two adjacent points was chosen to avoid overlapping of the areas affected. Both aggregate and cement areas at various

locations were tested, with examples with indenter markers shown in Fig. 12. Typical indenter depth – force curves for cement and aggregates are shown in Fig. 13. These curves were used to calculate elastic moduli using the Oliver and Pharr method (1992). The results are summarised in Table 1. The mean value of the Young's modulus for cement and aggregate is E_c=13.6 GPa and E_a=51.0 GPa, respectively; the values tend to decrease at high applied load, which may be caused by the cracking damage observable around indenters from Fig. 12b. The lower and upper limits of elastic moduli of the concrete cube are 23.1 GPa and 34.6 GPa, which were estimated using the Reuss and Voigt bounds (Hill, 1952):

$$E^{upper} = E_a F_a + E_c F_c \tag{1}$$

$$E^{lower} = \frac{E_a E_c}{E_c F_a + E_a F_c} \tag{2}$$
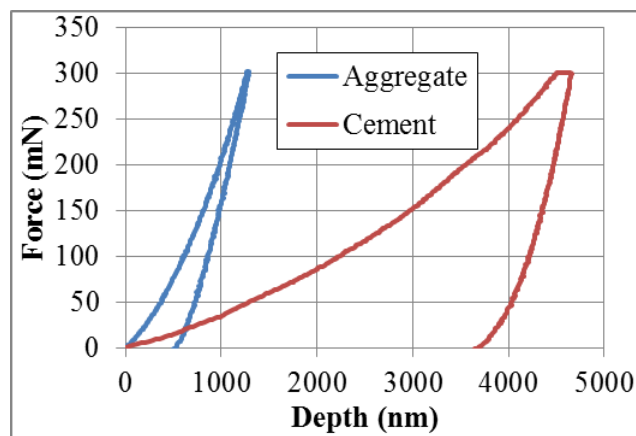
where F_a (=0.496) and F_c (=0.493) are the volume fraction of aggregates and cement, respectively, obtained from the segmented XCT images (section 3.3). The small void fraction of 1.1% by volume was neglected.
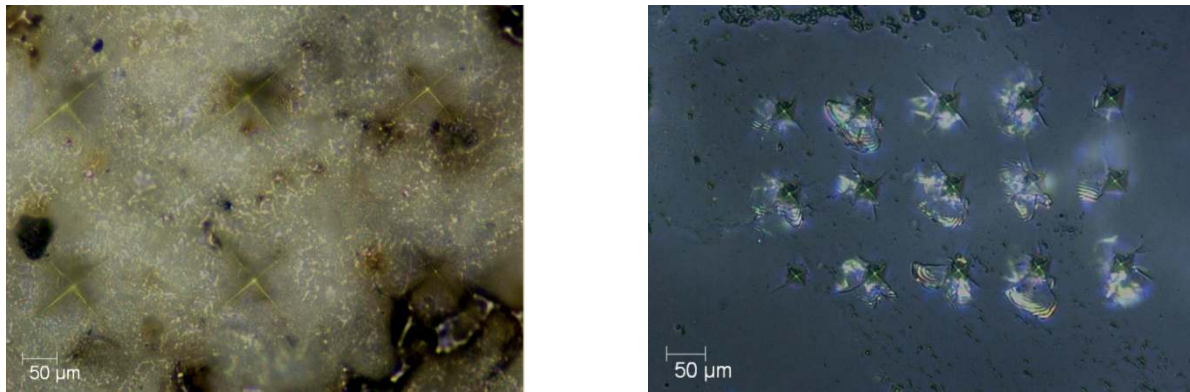
(a) Cement   (b) Aggregate

Fig. 12 Typical indents for cement and aggregate under 0.3N

Fig. 13 Typical indenter depth - force curves

Table 1 Young's moduli for aggregates and cement under different indentation forces

Maximum Force (N)		0.1	0.3	0.5	0.8	1	Average
E_a (GPa)	Mean	50.6	60.0	53.8	41.7	48.8	51
	Standard deviation	16.7	4.9	13.9	10.8	8.4	/
E_c (GPa)	Mean	12.0	16.2	16.2	13.3	10.3	13.6
	Standard deviation	3.4	2.5	4.3	2.7	2.2	/

3   XCT-IMAGE BASED NUMERICAL HOMOGENISATION

The method of asymptotic numerical homogenisation with periodic boundary conditions is one of the most effective approaches to obtain the effective homogenised stiffness matrix of a heterogeneous elastic material (Jansson 1992; Li 1997; Sharma et al. 2013). In this approach, six boundary conditions are applied to a representative volume element (RVE), which is modelled with detailed micro/meso-scale multi-phasic constituents, to calculate the homogenised elastic properties of the RVE.

The general constitutive relation in terms of asymptotic homogenization can be expressed as

$$\langle \sigma_{ij} \rangle = C_{ijkl}^{H} \langle \varepsilon_{kl} \rangle \tag{3}$$

where C_{ijkl}^{H} is the homogenised stiffness matrix. $\langle \sigma_{ij} \rangle$ and $\langle \varepsilon_{kl} \rangle$ are the volume-averaged stress and strain tensors, respectively

$$\langle \sigma_{ij} \rangle = \frac{1}{|V|} \left[\int_{V_c} \sigma_{ij}^{c} \, dV_c + \int_{V_a} \sigma_{ij}^{a} \, dV_a \right] \tag{4}$$

$$\langle \varepsilon_{ij} \rangle = \frac{1}{|V|} \left[\int_{V_c} \varepsilon_{ij}^{c} \, dV_c + \int_{V_a} \varepsilon_{ij}^{a} \, dV_a \right] \tag{5}$$

where V_c, V_a and V are the volume of cement, aggregate and the whole RVE, respectively.

The components of C_{ijkl}^{H} are obtained by applying six periodic boundary conditions one by one, with unit strain in one direction and zero strain in all other five directions. The details can be referred to Li (1997).

Four sizes of cubic RVEs, i.e., 10mm, 20mm, 30mm and 37 mm, cut from the segmented 3D concrete cube in Fig. 6d, were modelled. To investigate the effects of random distribution of internal phases, a few RVEs at different regions were used for each size: 5 for 10 mm (RVE10), 3 for 20 mm (RVE20), 2 for 30 mm (RVE30) and 1 for 37 mm (RVE7), as shown in Fig. 14. These XCT images were converted into FE meshes using the commercial software Simpleware (2011). The aggregates were smoothed before mesh generation to avoid too distorted elements. The FE

mesh for the 37 mm cube is shown in Fig. 15 as an example. It has 838,659 nodes and 2,942,955 tetrahedron elements. The Young's moduli of cement and aggregates (E_c=13.6 GPa and E_a=51.0 GPa) from the micro-indentation tests were used as basic inputs in all the simulations with Poisson's ratio assumed as 0.2 for both phases.
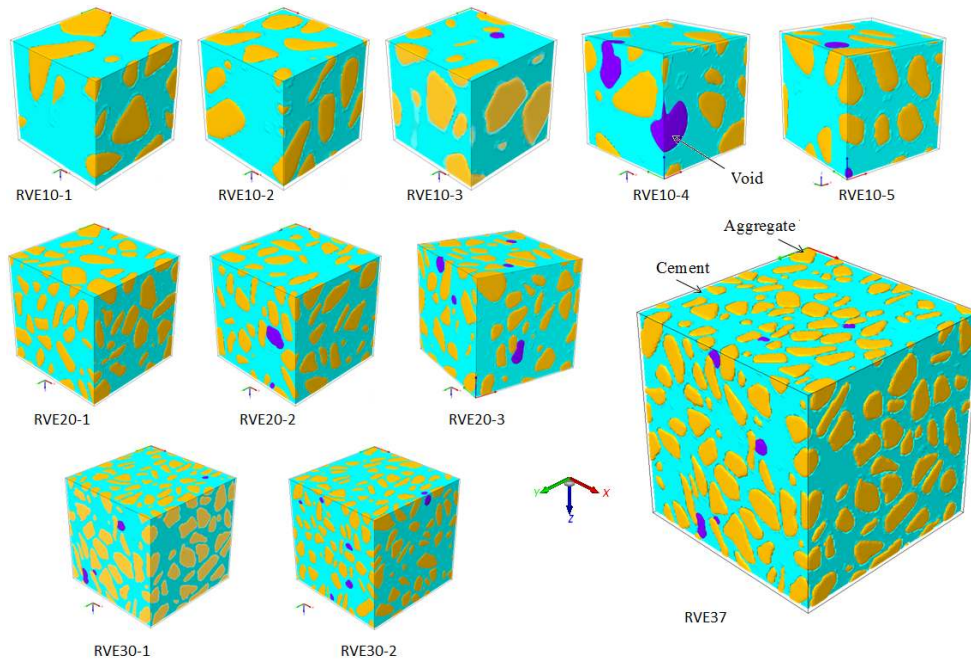

Fig. 14 The modelled RVEs (10mm, 20mm, 30mm and 37mm): aggregates in yellow, cement in green and voids in blue; not up to scale

Fig. 15 The finite element mesh for the 37mm concrete cube

All the 11 RVEs in Fig. 14 were simulated under the six loading conditions. Fig. 16 shows the stress contours of RVE10-1 (10mm) as an example. The stresses in the aggregates are higher than those in the cement for all loading conditions because they are much stiffer.
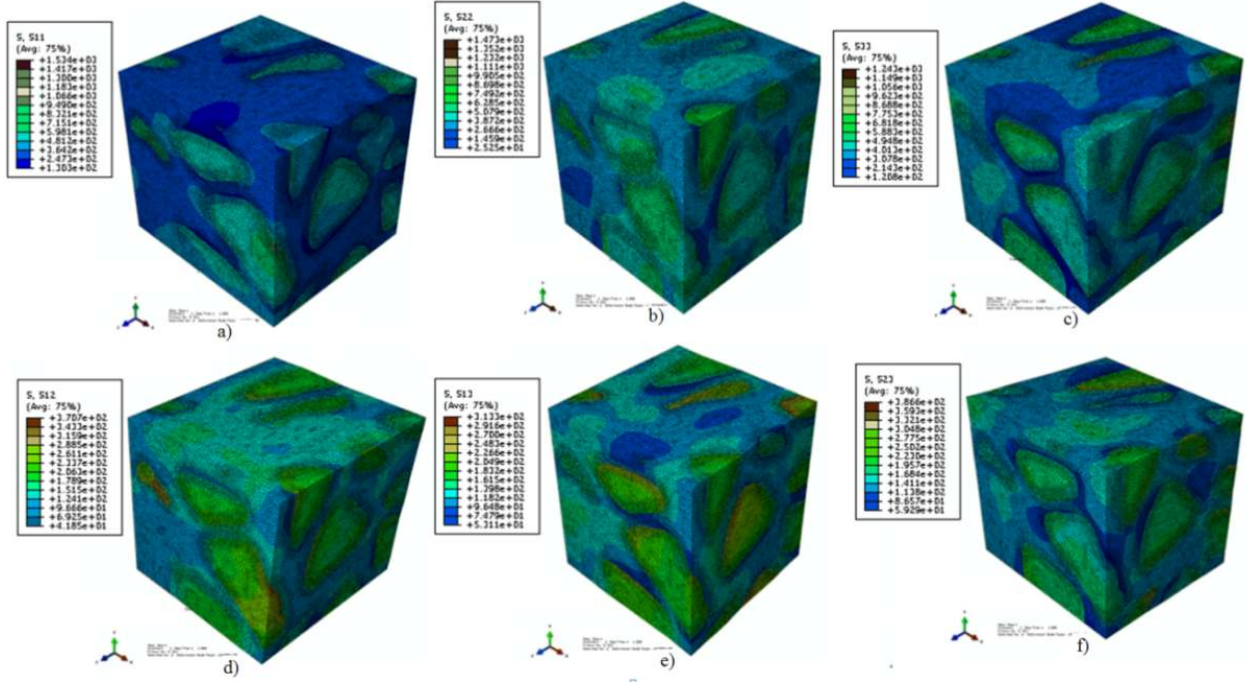
Fig. 16 Stress contours under six loading cases for RVE10-1

The homogenised stiffness coefficients of RVE10-1 are shown in Eq. 6. The coupling terms show that extension-shear and shear-shear components were much lower than those of extension-extension and were negligible.

$$
C_{ijkl}^{H} =
\begin{bmatrix}
26.77 & 6.74 & 6.73 & 0.12 & 0.48 & -0.015 \\
 & 27.57 & 6.70 & 0.30 & 0.16 & 0.23 \\
 & & 27.10 & 0.012 & 0.17 & -0.03 \\
 & & & 10.19 & 0.028 & 0.35 \\
 & \text{Symmetric} & & & 10.12 & 0.083 \\
 & & & \text{Shear-Shear} & & 10.20
\end{bmatrix}
\qquad (6)
$$

Extension-Extension   Extension-Shear

The calculated means and standard deviations for the five 10 mm RVEs are

$$
C_{ijkl}^{H} = \begin{bmatrix}
27.70 \pm 0.60 & 6.68 \pm 0.09 & 6.72 \pm 0.11 & 0 & 0 & 0 \\
& 27.37 \pm 0.44 & 6.72 \pm 0.07 & 0 & 0 & 0 \\
& & 27.58 \pm 0.68 & 0 & 0 & 0 \\
& \text{Symmetric} & & 10.12 \pm 0.12 & 0 & 0 \\
& & & & 10.20 \pm 0.20 & 0 \\
& & & & & 10.24 \pm 0.14
\end{bmatrix} \quad (7)
$$

All the components in Eq. 6 and Eq. 7 are in GPa. A clear cubical symmetry could be seen in Eq. 7, from which the elastic constants of the cube could be calculated. The elastic constants for all the RVE sizes are listed in Table 2, where the effective homogenised properties (EHP) are the volume averaged values of all the RVEs. The effective homogenised Young's modulus, shear modulus and Poisson's ratio of the concrete are 24.2 GPa, 10.0 GPa and 0.194, respectively. It can also be seen that the three normal constants differ slightly as well as the three shear constants, and thus the concrete cube in this study can be regarded as isotropic.

Table 1 Homogenised elastic constants

RVE size (mm)	E_{11} (GPa)	E_{22} (GPa)	E_{33} (GPa)	μ_{12}	μ_{13}	μ_{23}	G_{12} (GPa)	G_{13} (GPa)	G_{23} (GPa)
10	24.45 ± 0.58	24.72 ±0.43	24.91 ±0.65	0.2	0.2	0.2	10.11 ±0.13	10.19 ±0.20	10.23 ±0.14
20	24.19 ±1.05	24.73 ±1.08	24.96 ±1.28	0.195	0.193	0.195	10.08 ±0.47	10.15 ±0.46	10.30 ±0.48
30	23.67 ±0.35	24.40 ±0.37	24.47 ±0.38	0.194	0.194	0.195	9.93 ±0.13	9.97 ±0.15	10.15 ±0.16
37	23.58	24.22	24.38	0.194	0.193	0.194	9.92	9.95	10.11
EHP	23.67 ±0.21	24.33 ±0.22	24.47 ±0.24	0.194	0.193	0.194	9.94 ±0.08	9.98 ±0.09	10.14 ±0.09

4 CONCLUSIONS

A suite of advanced experimental and numerical techniques have been used to study the complicated 3D progressive failure and evaluate the elastic properties of concrete cubes. The main conclusions are

(1) the in-situ micro XCT testing technique together with image analyses by digital volume correlation (DVC) offers a new potential to observe complicated 3D fracture paths in multi-phasic materials like concrete;

(2) two methods have been used to quantify and visualise the fracture evolution as the deformation increases. The threshold-based segmentation procedure is able to separate the concrete into three distinguished phases and visualise directly the development of major cracks. Damage may

be quantified by the variation of volume fraction of cracks and voids. The DVC technique maps the relative deformations between consecutive XCT images with high precision; bulk deformation can be measured and cracks visualised indirectly via their opening displacement or strain. The 3D crack profiles obtained by the two methods are comparable. The segmented microstructures can be used as inputs for image-based FE models, and the displacements and strains from the DVC analyses of segmented XCT data may be used to validate predictions of these models;

(3) the XCT-image based FE models have been successfully used in asymptotic homogenisation. The homogenised elastic modulus is 24.2 GPa, which is close to the experimentally obtained 26.42 ± 3.20 GPa using the DVC analysis of displacements. This is within the Ruess-Voigt theoretical bounds (23.1-34.6GPa) calculated using the Young's moduli of cement and aggregates obtained from the micro-indentation tests; and

(4) a combined use of these advanced techniques, including the in-situ micro-XCT, micro-indentation, DVC and image-based modelling, offers highly-accurate, complementary functionalities for both qualitative understanding of complicate 3D damage and fracture evolution and quantitative evaluation of elastic material properties of multi-phasic composite materials such as concrete.

REFERENCES

AVIZO. AVIZO User's Guide, 2013.

Babout L, Marrow TJ, Engelberg D, Withers PJ. X-ray microtomographic observation of intergranular stress corrosion cracking in sensitised austenitic stainless steel. Materials Science and Technology. 2006; 22: 1068-1075.

Baimpas N, Xie M, Song Xu, Hofmann F, Abbey B, Marrow J, et al. Rich tomography techniques for the analysis of microstructure and deformation. Int J Comput Methods 2014; 11: 1343006.

Bay BK et al, Digital volume correlation: three-dimensional strain mapping using X-ray tomography. Experimental Mechanics. 1999. 39(3): 217-226.

Bay BK, Smith TS, Fyhrie DP and Saad M. Digital volume correlation: Three-dimensional strain mapping using x-ray tomography. Experimental Mechanics, 1999;39 (3): 217–226.

Cai B, Lee PD, Karagadde S et al. Time-resolved synchrotron tomographic quantification of deformation during indentation of an equiaxed semi-solid granular alloy. Acta Material., 2016; 105: 338–346.

Carlson WD. Three-dimensional imaging of earth and planetary materials. Earth and Planetary Science Letters. 2006; 249: 133-147.

DaVis. User's Manual. Gottingen: LaVision GmbH. 2012

De Kock, T, Boone, MA, De Schryver, M，Van Stappen, J et al, A pore-scale study of fracture dynamics in rock using X ray MicroCT under ambient freeze−thaw cycling, Environmental Science and Technology. 2015; 49: 2867−2874.

Drummond JL, De Carlo F, Super BJ. Three-dimensional tomography of composite fracture surfaces. Journal of Biomedical Materials Research Part B: Applied Biomaterials. 2005;74B:669-675.

Garboczi EJ. Three-dimensional mathematical analysis of particle shape using X-ray tomography and spherical harmonics: Application to aggregates used in concrete. Cement and Concrete Research. 2002; 32: 1621-1638.

Gonzalez D, King A, Mostafavi M, Reischig P, du Roscoat SR, Ludwig W, et al. Three-dimensional observation and image-based modelling of thermal strains in polycrystalline alumina. Acta Mater 2013; 61: 7521−7533.

Hill R. The elastic behaviour of a crystalline aggregate. Proceedings of the Physical Society. Section A, 1952: 65(5), 349.

Hollister SJ, Kikuchi N. 1994. Homogenization theory and digital imaging: a basis for studying the mechanics and design principles of bone tissue. Biotechnology and Bioengineering 1994: 43 (7), 586-596.

Jansson S. Homogenized nonlinear constitutive properties and local stress concentrations for composites with periodic internal structure. International Journal of Solids and Structures. 1992: 29, 2181-2200,

Kassner ME et al., New directions in mechanics. Mechanics of Materials. 2005. 37:231-259.

Kerckhofs G, Schrooten J, Van Cleynenbreugel T, Lomov SV, Wevers M. Validation of x-ray microfocus computed tomography as an imaging tool for porous structures. The Review of scientific instruments. 2008; 79: 013711.

Landis EN, Bolander JE. Explicit representation of physical processes in concrete fracture. Journal of Physics D: Applied Physics 42, 2009, 214002 (17pp).

Li S. On the unit cell for micro mechanical analysis of fiber reinforced composites. Proceedings of Royal Society London. 1997: 54, 815−838.

Li Y. Characterisation of 3D Cracks in Concrete from XCT Images. MSc thesis, School of Mechanical, Aerospace and Civil Engineering, the University of Manchester, 2012.

Man HK, van Mier JG. Size effect on strength and fracture energy for numerical concrete with realistic aggregate shapes. International Journal of fracture, 2008: 154(1-2), 61-72.

Marrow TJ, Babout L, Jivkov AP, Wood P, Engelberg D, Stevens N, et al. Three dimensional observations and modelling of intergranular stress corrosion cracking in austenitic stainless steel. Journal of Nuclear Materials. 2006; 352: 62-74.

Marrow TJ, Liu D, Barhli SM, Saucedo-Mora L, Vertyagina Y, Collins DM, et al. In situ measurement of the strains within a mechanically loaded polygranular graphite. Carbon 2016; 96: 285−302.

Marrow TJ, Mostafavi M, Hashimoto T, Thompson GE. A quantitative three-dimensional in situ study of a short fatigue crack in a magnesium alloy. Int J Fatigue 2014; 66: 183−193.

McDonald SA, Dedreuil-Monet G, Yao YT, Alderson A, Withers PJ. In situ 3D X-ray microtomography study comparing auxetic and non-auxetic polymeric foams under tension. Physica Status Solidi (b) 2011: 248, 45-51.

Meyer D, Man HK, van Mier JG. Fracture of foamed cementitious materials: a combined experimental and numerical study. In IUTAM Symposium on Mechanical Properties of Cellular Materials, 2009, 115-123. Springer Netherlands,

Mostafavi M, Baimpas N, Tarleton E, Atwood RC, McDonald SA, Korsunsky AM, et al. Three-dimensional crack observation, quantification and simulation in a quasi-brittle material. Acta Mater 2013a; 61: 6276−6289.

Mostafavi M, McDonald SA, Mummery PM, Marrow TJ. Observation and quantification of three-dimensional crack propagation in poly-granular graphite. Eng Fract Mech 2013b; 110: 410–20.

Mostafavi M., Collins D.M., Cai B., Bradley R., Atwood R.C., Reinhard C., et al., Yield behavior beneath hardness indentations in ductile metals, measured by three-dimensional computed X-ray tomography and digital volume correlation, Acta Mater. 2015; 82: 468–482.

Nagira T, Gourlay CM, Sugiyama A et al. Direct observation of deformation in semi-solid carbon steel, Scripta Materialia, 2011; 64(12): 1129-1132.

Oden JT et al, Research directions in computational mechanics. Computer Methods in Applied Mechanics and Engineering. 2003. 192:913-922.

Oliver WC, Pharr GM. An improved technique for determining hardness and elastic modulus using load and displacement sensing indentation experiments. Journal of Materials Research, 1992: 7(06), 1564-1583.

Qian L, Toda H, Uesugi K, Ohgaki T, Kobayashi M, Kobayashi T. Three-dimensional visualization of ductile fracture in an Al–Si alloy by high-resolution synchrotron X-ray microtomography. Materials Science and Engineering: A. 2008; 483–484: 293-296.

Qsymah A., Sharma R., Yang Z.J., Margetts L., McDonald S., XCT Image-based homogenisation of the elastic properties of ultra high performance fibre reinforced concrete; 23rd Conference of the Association for Computational Mechanics in Engineering, ACME-UK; Swansea, UK. 2015.

Saucedo-Mora L, Mostafavi M, Khoshkhou D, Reinhard C, Atwood R, Zhao S, et al., Observation and simulation of indentation damage in a SiC–SiC fibre ceramic matrix composite, Finite Elem. Anal. Des.2016; 110:11–19.

Sharma R, Mahajan P, Mittal RK. Elastic modulus of 3D carbon/carbon composite using image-based finite element simulations and experiments. Composite Structures. 2013; 98: 69-78.

Simpleware. ScanIP, +FE and +CAD Version 4.3 Reference Guide. Exeter, UK: Simpleware Ltd, 2011.

Song S, Paulino G, Buttlar W. Simulation of Crack Propagation in Asphalt Concrete Using an Intrinsic Cohesive Zone Model. Journal of Engineering Mechanics. 2006; 132: 1215-1223.

Terada K, Miura T, Kikuchi N. Digital image-based modelling applied to the homogenization analysis of composite materials. Computational Mechanics 1997: 20 (4), 331-346.

Vertyagina Y, Mostafavi M, Reinhard C, Atwood R, Marrow TJ. In situ quantitative three-dimensional characterisation of sub-indentation cracking in polycrystalline alumina. J Eur Ceram Soc 2014;34: 3127–3232.

Wang LB, Frost JD, Voyiadjis GZ, Harman TP. Quantification of damage parameters using X-ray tomography images. Mechanics of Materials. 2003; 35: 777-790.